Jet turbulence characteristics associated with downstream and sideline sound emission

F. Kerhervé,* P. Jordan,* J. Delville,*
C. Bogey† & D. Juvé†

A tool based on Linear Stochastic Estimation and frequency-wavenumber filtering, aimed at clarifying the flow characteristics associated with sideline and downstream sound emission from subsonic jets, is presented. The wavenumber-frequency filter is first used to separate components radiating in two angular sectors: (0° $\leq \theta \leq$60°) and (60° $\leq \theta \leq$120°). Flow variables (pressure and velocity) are correlated with the pressure fluctuations observed in each of these sectors and conditional space-time flow fields associated with the two radiation sectors are then computed by means of stochastic estimation. An analysis of the conditional flow fields is presented. The three main results of the analysis are, for the flow we study: (1) the radiating sub-space of the jet shows a higher degree of organisation than the turbulence which drives it (using the POD eigenspectrum convergence as a metric of this organisation we find an order of magnitude difference between the full flow solution and the radiating flow skeleton); (2) organised large-scale flow motion is important for both downstream and sideline sound emission (though this may be due, in part, and particularly where sideline radiation is concerned, to the overly coherent nature of the LES solution); (3) a wavepacket mechanism associated with coherent structures is observed where downstream radiation is concerned.

I. Introduction

We do not presently understand what it is about a jet that leads to the angle-dependent spectral shapes of the radiated sound field. In this paper we propose a tool aimed at shedding some light on the question. The technique is based on a frequency-wavenumber filtering of the radiated pressure field, which allows us to separate pressure fluctuations propagating in different directions, followed by an application of Linear Stochastic Estimation, as proposed by Adrian.[1] By means of stochastic estimation, which has proved extremely useful in the study of 'coherent structures' in turbulence,[2–4] an estimate of the conditional average $< \vec{q}'(\vec{x},t)|E(\vec{y},t+t_E) >$ can be obtained, where $\vec{q}'(\vec{x},t)$ is the turbulent flow quantity considered (vorticity, velocity, pressure, temperature,...), and the conditional average is with respect to the event $E(\vec{y},t+t_E)$. In this paper we specify two event vectors, $E_{30}(\vec{y},t+t_E)$ and $E_{90}(\vec{y},t+t_E)$, corresponding, respectively, to pressure fluctuations radiated to low and high angles (measured from the downstream jet axis). Stochastic estimation is applied in an adapted form such that the retarded-times $t_E(\vec{x},\vec{y})$, between a grid of points distributed over the flow domain, $\vec{x}$, and a second grid of points distributed over the acoustic domain $\vec{y}$, are accounted for. These retarded times are computed by means of a ray-tracing algorithm, so as to correctly account for mean-flow refraction effects.

If we consider the jet noise problem to comprise two major challenges, one kinematic and one dynamic, the tool we describe here is aimed at tackling the first of these. The kinematic part of the problem arises on account of the large range of acoustically inefficient flow scales which make up a turbulent jet on one hand, and, on the other, because of the absence of a universally accepted theory of jet noise: it is not clear how to define and/or visualise the coupling between a (given) turbulent shear flow and the sound field which it radiates, even when full space-time data is available. If the sound-producing motions are clarified, progress is made with regard to the kinematic part of the problem, and questioning can begin with respect to the dynamics: what is the dynamic law (which we hope is simpler than the dynamical system described by the full Navier Stokes equations) of the fluid kinematics which are associated with sound production? Examples of reduced-complexity dynamical systems are: Large Eddy Simulation, linear and non-linear stability approaches (Parallel-flow stability analysis; Parabolised Stability Equations; Global stability analysis,...), POD-Galerkin models. By focusing on the kinematics, as we do in this paper, we aim to equip ourselves with a mechanistic understanding which can guide the conception (or best-choice, in the case where one of the existing models proves to be appropriate) of a reduced-complexity dynamical model.

*Institut Pprime, CNRS UPR 3346, Université de Poitiers, ENSMA, France
†Laboratoire de Mécanique des Fluides et d'Acoustique, CNRS UMR 5509, Ecole Centrale de Lyon, France

The results presented in this paper show that the sound-producing sub-space of the turbulent jet is more organised than the turbulence which drives it; this conclusion is in agreement with the previous study of Jordan et al.,[5] and suggests that reduced-complexity dynamical modelling may be appropriate for jet noise. Furthermore, for the flow analysed we demonstrate how the sideline radiation is associated with flow scales which are in fact larger than those associated with downstream radiation. In our particular study, this result may be an artefact of the overly coherent nature of the LES solution; however, the fact that sideline radiation by unsteady vortex dynamics can be characterised by such large scales is, in itself, an interesting observation.

Finally, study of a short-time evolution of the conditional flow fields shows that the downstream radiation can be understood in terms of a wavepacket mechanism—this suggests that the Parabolised Stability Equations may constitute a pertinent dynamical model for this component of the source mechanism.

II. Flow configuration

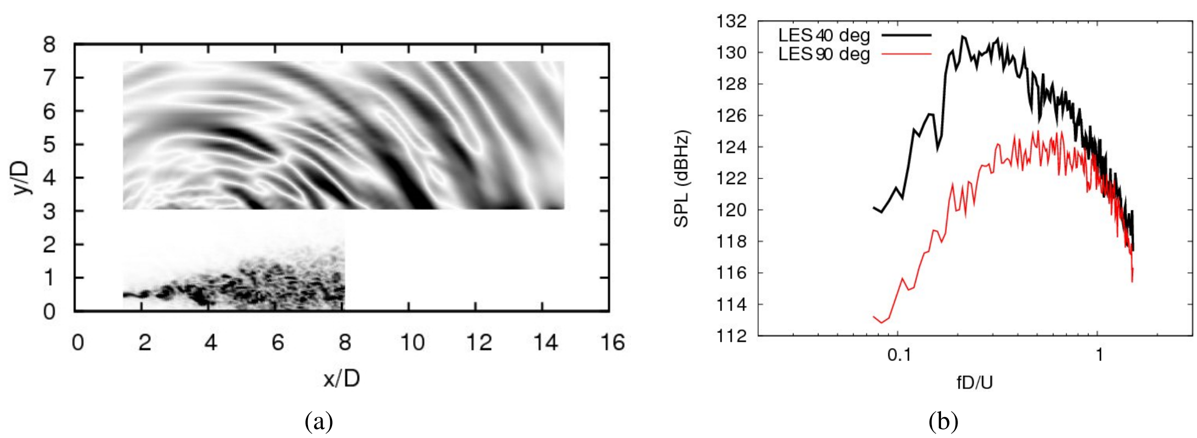

Figure 1. (a) Snaphot of vorticy field and radiated pressure contours of the single Mach 0.9 jet; (b) Acoustic pressure spectra at different emission angles

The flow investigated is a Mach 0.9 single-stream jet with Reynolds number of 4×10^5, obtained from the Large Eddy Simulation of Bogey $\&$ Bailly.[6] Details of the simulation can be found in Bogey $\&$ Bailly.[6–8] Flow and sound properties of this single-stream jet case have been extensively detailed in the literature. For the present study, the flow region is described by a mesh of 100×71 points, extending axially from x/D=1.5 to x/D=8 (D denotes the nozzle diameter) and radially from y/D=0 to y/D=3, while the mesh for the radiated pressure field consists of 137×35 points extending axially from x/D=1.5 to x/D=14.5 and radially from y/D=3 to y/D=7. Snaphots of the vorticty and radiated pressure fields are shown in figure 1(a). Sound spectra measured at 40° and 90° are shown in figure 1(b). We see here that, on account of both the unresolved scales and the fact that the upstream boundary layer has not been simulated, the sideline spectra is peakier than that observed experimentally. A total number of N_p =19000 snaphots, sampled at 60kHz (which corresponds to a Strouhal number of $St_D = 3.9$), are considered; this number has been found sufficient for the obtention of converged flow-flow and flow-acoustic correlations.

III. Directional filtering of the radiated sound field

The directive character of the sound field radiated by a round jet is sometimes argued to be due to the action of coherent structures (Tam et al[9]). However, it is not possible to provide a precise definition of what is meant by 'coherent structure' nor is it clear which aspects of their motion lead to the directive sound field produced by the round jet (this is discussed in some detail by Jordan and Gervais[10]). Our aim is to equip ourselves with a tool which can help provide some clarification on this point.

The methodology proceeds as follows. We begin by filtering the radiated pressure field into two angular sectors (0° $\leq \theta \leq$60°) and (60° $\leq \theta \leq$120°), which we will henceforth refer to, respectively, as $E_{30}(\vec{y},t)$ and $E_{90}(\vec{y},t)$. This filtering is effected in frequency-wavenumber space, (k_x,ω), for each radial position y/D. A bandpass filter is used, which, for a given frequency, retains wavenumbers in the range $\omega/c(\theta_1) < k_x < \omega/c(\theta_2)$ where c$(\theta_i) = c_o/\cos(\theta_i)$

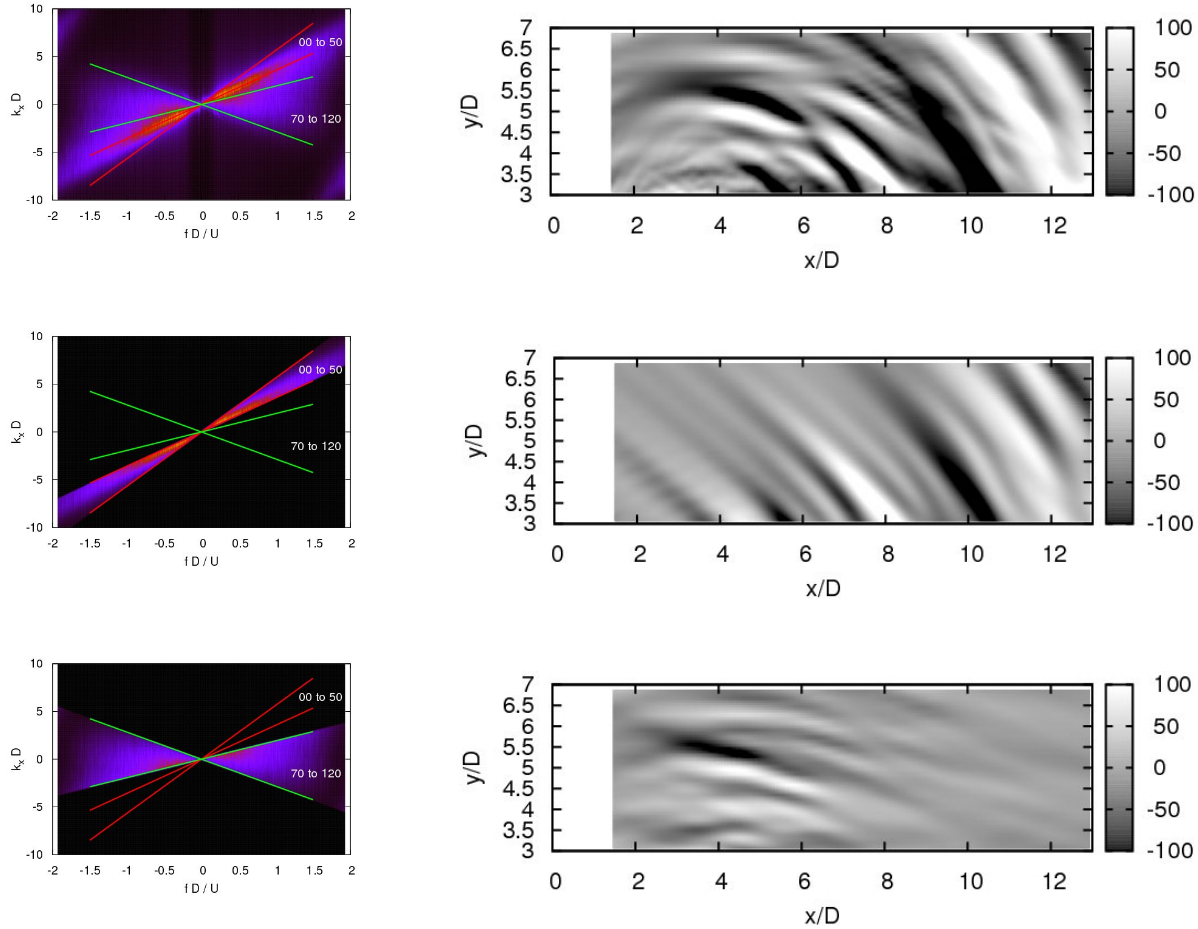

(a) (b)

Figure 2. (a) Wavenumber-frequency energy spectrum associated with (top) overall radiated pressure field (bottom) pressure field in angular segment (middle) 0°-60° and (bottom) 60°-120°. (b) Associated snapshots of the radiated pressure fields.

and θ_i denotes the angular segments of interest. The following windowing function is applied:

$$W(k_i, \omega) = \frac{1}{2}\left[\tanh\left(\alpha \frac{k_i - |\omega|/c(\theta_1)}{|\omega|/c(\theta_1) - k_N}\right) + \tanh\left(\alpha \frac{k_i - |\omega|/c(\theta_2)}{|\omega|/c(\theta_2) + k_1}\right)\right] \text{ for } i = 1, .., N. \quad (1)$$

Figure 2 shows frequency-wavenumber (left column) and space-time (right column) representations of the full pressure field (top), the $E_{30}(\vec{y}, t)$ component (middle) and the $E_{90}(\vec{y}, t)$ component (bottom). Both filtered fields exhibit a broad range of acoustic scales, but the $E_{90}(\vec{y}, t)$ manifests a lower degree of organisation. We will be interested in identifying, by means of stochastic estimation, the conditional flow fields associated with each of these components of the radiated pressure fluctuations.

IV. Linear Stochastic Estimation

Stochastic estimation provides a means by which an approximation can be obtained for the conditional space-time flow fields, $\hat{q}_{30}(\vec{x}, t) =< q(\vec{x}, t)|E_{30}(\vec{y}, t + t_E) >$ and $\hat{q}_{90}(\vec{x}, t) =< q(\vec{x}, t)|E_{90}(\vec{y}, t + t_E) >$. These can be computed

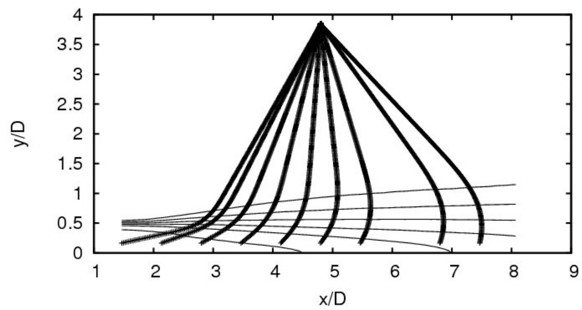

Figure 3. Bold lines: acoustic ray paths between a selection of points in the flow region and a point in the acoustic field. Thin lines: isocontours of mean axial velocity.

as follows:

$$\hat{q}(\vec{x},t) = \sum_{j=1}^{N} A_j(\vec{x}) p_j(t + t_{E_j}(\vec{x})) \tag{2}$$

$$\tag{3}$$

where the coefficients A_j in equation Eq.(3) are obtained by solving the linear system of equations:

$$\begin{bmatrix} \overline{q(\vec{x},t)p_1(t+t_{E_1}(\vec{x}))} \\ \vdots \\ \overline{q(\vec{x},t)p_N(t+t_{E_N}(\vec{x}))} \end{bmatrix} = \begin{bmatrix} \overline{p_1(t)p_1(t)} & \dots & \overline{p_N(t)p_1(t+t_{E_1}(\vec{x})-t_{E_N}(\vec{x}))} \\ \vdots & \ddots & \vdots \\ \overline{p_1(t)p_N(t+t_{E_N}(\vec{x})-t_{E_1}(\vec{x}))} & \dots & \overline{p_N(t)p_N(t))} \end{bmatrix} \begin{bmatrix} A_{j1} \\ \vdots \\ A_{jN} \end{bmatrix}. \tag{4}$$

$\overline{p_i(t)p_j(t+\tau)}$ and $\overline{q(\vec{x},t_q)p_j(t+\tau)}$ are, respectively, acoustic/acoustic and flow/acoustic time-averaged correlations. $N = 20 \times 7$ pressure sensors are considered, and these are regularly distributed over the radiated field. The retarded time $\tau_{E_j}(\vec{x})$ is computed, between the flow point $\vec{x}$ and the microphone sensor p_j, by solving the ray-tracing equations, following the procedure described by Bogey & Bailly.[11] A fourh-order Runge-Kutta scheme is used for temporal integration of the equations while mean flow derivatives are calculated using centered fourth-order finite-differences. Samples of calculated ray paths are shown in figure 3, giving a sense of the effect of mean-flow refraction.

V. Results and discussion

A. Instantaneous fields

Figure 4(a) shows the full LES solution, at a given instant in time, over a spatial domain extending from $x/D = 1.3$ to $x/D = 14.5$ and from $y/D = 0$ to $y/D = 7$. The domain has been divided into three regions: A, B & C. The pressure time histories of two pressure 'probes' located in zone A, respectively, at $(x/D, y/D) = (10, 4)$ and $(3, 4)$ (shown by the black and red squares) are also shown in the bottom right hand corner of the top image. These are helpful for tracking acoustic signatures to and from the flow—an example of this kind of analysis is presented later.

In zone A we consider the pressure field, which is here entirely propagative. In zone B we consider the nearfield pressure, which comprises both propagative and non-propagative components; the latter, which carry the footprint of coherent structures (Tinney & Jordan[12]), are frequently considered synonymous with linear instability waves (Suzuki & Colonius[13]) and have inspired a number of reduced-complexity source modelling methodologies (Gudmundsson et al.,[14] Sandham et al[15]). Finally, in zone C we consider the velocity vector field (as seen in the (x, y) plane), indicated by the black arrows. In order to aid in the visualisation of the results the velocity field is viewed, as per Picard & Delville,[16] as $\alpha u' + \overline{U} - U_C$ with $\alpha = 10$ and $U_C = 0.55U_J$; i.e. we view the flow in a Lagrangian reference frame, convected at velocity U_c, and by means of the coefficient α we boost the level of the fluctuation so as to more clearly discern the topology of the flowfield. The red lines in zones B and C are isocontours of zero pressure; by means of these we can identify regions of positive and negative pressure within zone C, i.e. the extension of zone B into the non-linear, rotational region of the flow.

Figure 4(b) shows, in zones B and C, the instantaneous conditional pressure and velocity fields, computed by means of Linear Stochastic Estimation, where the complete LES solution in zone A has been used as the event vector; i.e. we

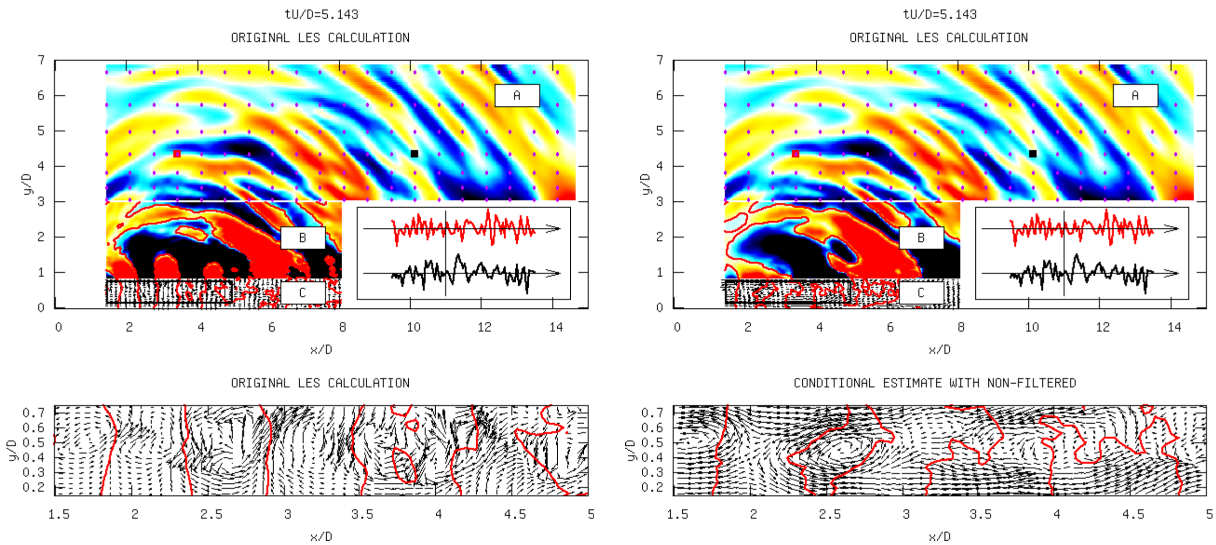

(a) (b)

Figure 4. (a) LES solution; (b) zone A: LES solution (acoustic pressure); zone B: conditional near pressure field; zone C: conditional velocity field. Bottom figure shows zoom of the region delimited by black box in zone C. Blue and red shadings correspond, respectively, to low and high pressures. The red line in zone B is an iso-contour of zero pressure.

have not, for the moment, implemented the directional filtering. It is important to note that the conditional pressure and velocity fields are computed independently, via pressure-pressure and pressure-velocity correlations, respectively. A first observation which can be made regarding the conditional field is that we obtain perfect continuity between zones A and B (remember, zone B in figure 4(b) comprises an instantaneous *cliché* of the reconstructed field, while zone A is the LES solution), and this continuity persists as we evolve the estimate and LES solution in time. This perfect continuity is due to the fact that the relationship between pressure fluctuations at $y/D > 3$ and those in the region $2 < y/D < 3$ is purely linear; as we approach the non-linear region of the flow we see a progressive increase in the difference between the conditional fields and the full LES solution. These are the differences which we are interested in: the conditional fields we compute constitute structural entities which are related to the sound field by means of an optimal linear transfer function; we can thus think of them as comprising a reduced-complexity sub-space of the flow which is linearly mapped to the sound field.

Examination of the conditional velocity field in figure 4(b) shows it to be more organised than the full LES solution: we see large, axially organised, vortical structures (at $x/D = 1.6, 2.5, 3.7$), interspersed by a series of saddle points ($x/D = 2, 3.2$). Furthermore, we see that the regions of negative and positive conditional pressure (which is computed independently of the velocity field) correspond, as one would expect, to the vortical cores and the saddles points. This result is reminiscent of those obtained by the turbulence community in their attempts to separate 'coherent structures' from 'background turbulence' in various turbulent shear flows (see Adrian[1]). However, in the present study, rather than using event data associated with turbulence quantities, we have used the radiated sound field.

We now turn our attention to the question regarding the flow subspaces associated with downstream and sideline sound emission. Figure 5 shows the result of the frequency-wavenumber filtering (outlined earlier), applied in zone A. In this figure zones B and C show the full LES solution. Figures 5(c) & (d) show, in zones B and C, the conditional fields, associated, respectively, with E_{30} and E_{90}; the full LES velocity field has been included for comparison. The perfect continuity, observed between zones A and B when the full LES information was used in zone A to perform the conditional estimate, is no longer observed: there are some small discrepancies in pressure amplitude. These can be explained by the filtering operation which was used to decompose the full LES data into E_{30} and E_{90}. The windowing function defined by equation 1 removes a certain amount of information close to the line which demarcates the E_{30} region of frequency wavenumber space from the E_{90} region. This contamination leads to a slight degradation of the correlation between the acoustic pressure fluctuations and the flow quantities.

The conditional near pressure field (zone B) associated with downstream radiation shows a marked wavepacket type structure, where both convective and propagative signatures are manifest (this is clearer when we look at the animations). The associated conditional velocity field again shows, clearly, an axial distribution of vortical structures and saddle points, which carry with them (convective) low and high pressures (the red lines show how the nearfield

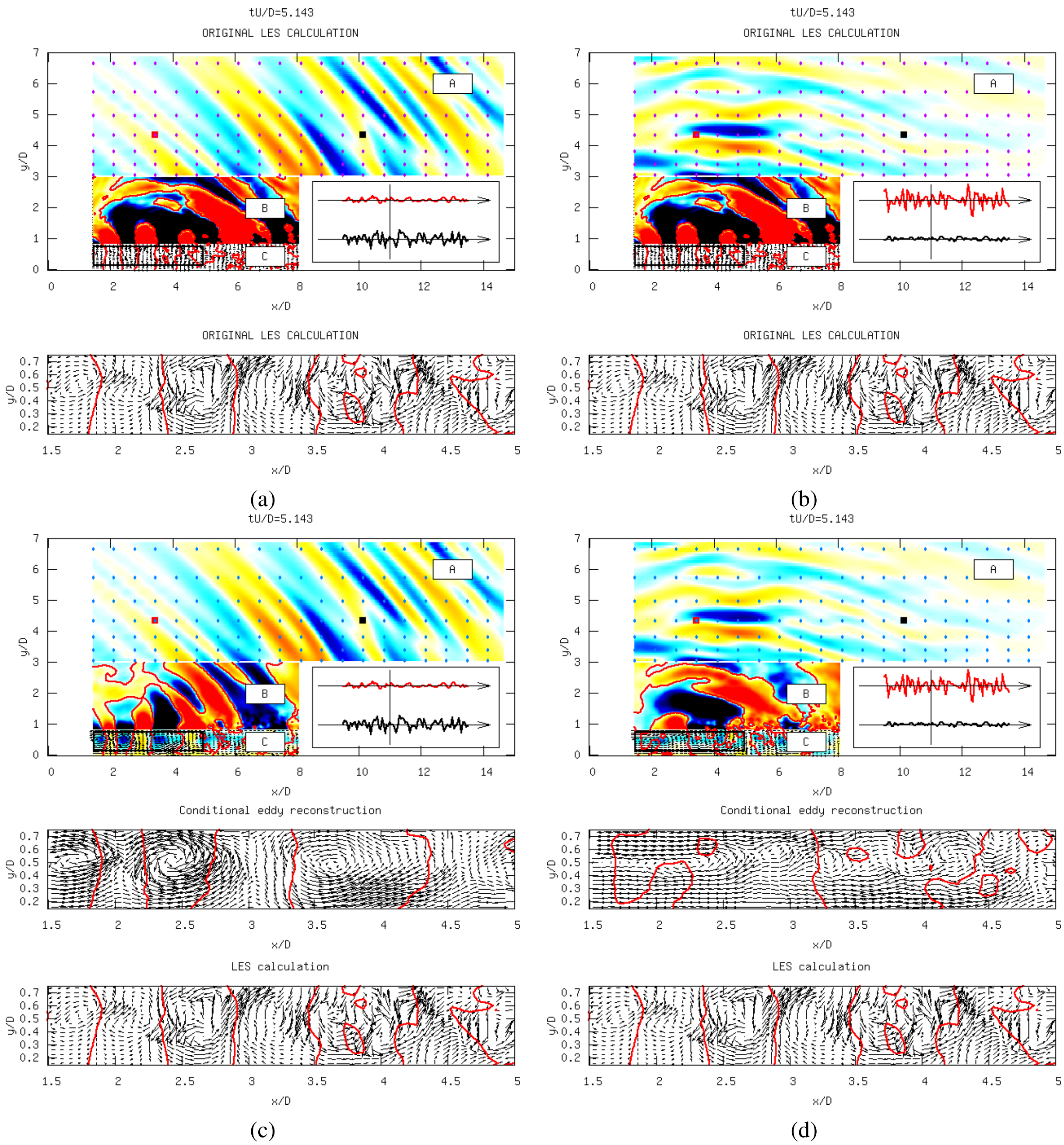

Figure 5. (a) zone A: E_{30}; zones B & C: LES solution (pressure and velocity, respectively); (b) zone A: E_{90}; zones B & C: same as (a); (c) zone A: E_{30}; zones B & C: associated conditional pressure and velocity fields; (d) zone A: E_{90}; zones B & C: associated conditional pressure and velocity fields for E_{90}

carries the signature of these structures). Study of the animations shows how the transition from convective to propagative pressure in the nearfield (which is manifest in figure 5(c)) is often associated with a rupture of the space-time homogeneity of the organisation of the vortical structures (respectively, saddle points) and the convective depressions (respectively, high-pressure) which they carry; we provide some examples in section C. Where sideline radiation is concerned the conditional fields are less straightforward to interpret. Organised vortical structures and saddle points can be observed, and these again carry low and high pressures. However, the axial alignment of these is not as marked as the E_{30} fields; they tend, rather, to organise themselves into axially elongated 'blobs', and the moments at which large propagative pressures are observed in the conditional nearfield (and which continue to propagate outward where they eventually become the filtered farfield data) correspond, again, to the axial inhomogeneities comprised by these blobs: when two axially extended regions of low pressure (vortical motion) are separated by a reduced region of high pressure (small saddle point), the low pressures tend to form a bridge above the high-pressure zone, and this bridge then propagates to the farfield. An example of this can be seen in figure 5(d) (large depression, shown in blue, at approximately $y/D = 1.5$ and extended axially between $x/D = 2.2$ and $x/D = 4.7$). One again gets the impression that the sound production mechanism can be associated with a wavepacket like motion, but one in which the convective character of the field is not the essential feature. Something which is clear is that the sideline radiation is underpinned, in this flow, by coherent structures with similar scales as those which drive downstream propagation. Some examples will be given in what follows.

These initial observations raise the question as to whether it makes sense to think of sound production in free jets as being driven by two distinct mechanisms; however, this comment must be accompanied by the caveat that what we are looking at is Large Eddy Simulation, where much of the smaller-scale activity is missing and where the inlet conditions are not realistic. We nonetheless observe coherent vortical structures which radiate in the sideline directions at higher frequencies than the downstream emission; the fact that coherent large-scale motions can radiate in this way is, in itself, an interesting observation.

B. Statistical evaluation of conditional-flow organisation

In this section we present the results of a Proper Orthogonal Decomposition of the conditional flow fields presented in the previous section. The Fredholm integral eigenvalue problem,

$$\sum_{j=1}^{N_c} \int_D R_{ij}(X, X')\Phi_j^{(n)}(X')dX' = \lambda^{(n)}\Phi_i^{(n)}(X) \tag{5}$$

is solved. $R_{ij}(X, X')$ represents a two-point correlation tensor of the velocity field, N_c the number of components used to describe the velocity, $\lambda_{(n)}$ and $\Phi_i^{(n)}$ are, respectively, the eigenvalue and spatial eigenfunctions of a given realisation. The vectorial snapshot formulation introduced by Sirovich (1987) is here implemented; the kernel is spatially averaged:

$$R_{ij} = \frac{1}{N_c n_x n_y} \sum_{k=1}^{N_c} \sum_{l=1}^{n_x} \sum_{m=1}^{n_y} u_k(X_{lm}, t_i) u_k(X_{lm}, t_j) \tag{6}$$

where n_x and n_y are the spatial dimensions of the velocity field. The POD coefficients are obtained by solving the eigenvalue problem:

$$Ra^{(n)}(t) = \lambda^{(n)} a^{(n)}(t), \tag{7}$$

and the eigenfunction are obtained by projection of these coefficients onto the velocity field:

$$\Phi_k^{(n)}(X) = \sum_{i=1}^{i=N_t} a^{(n)}(t_i) u_k(X, t_i) \quad \text{with } k = 1, .., N_t. \tag{8}$$

Two POD metrics are used in order to assess the topological character of the conditional velocity fields: the convergence of the POD eigenspectrum is used to assess the degree of spatial organisation, while the POD eigenfunctions gives us an idea of the representative spatial scales and their topology. Figure 6 shows the POD eigenspectra corresponding to the full LES data, the E_{30} conditional velocity field and the E_{90} field. The result is clear: the complexity of the complete LES data leads to an eigenspectrum with slow convergence (100 modes required to capture 60% of the fluctuation energy), while the more organised structure manifest in the E_{30} and E_{90} fields is reflected in a more rapid convergence (10 modes to capture the same amount of energy). This order of magnitude difference between the full LES data and the conditional fields provides a nice illustration of how the sound-producing structure of a jet is less complex than the turbulence which drives it. In order to be sure that the convergence is not sensitive to the number of sensors used to perform the LSE, we present in figure7 the convergence of the POD eigenspectrum for conditional pressure fields (estimated in zones B and C) using two grid densities in zone A. Despite a doubling of the number of conditional probes the convergence remains the same.

The POD eigenfunctions are presented in figure 8. These figures give a sense of the spatial characteristics of the two conditional flow fields. As we saw previously, despite the higher frequency of the E_{90} sound field (see figure1(b)), the spatial scales of the E_{90} conditional velocity field are clearly larger than those of the E_{30} field. The physical trait

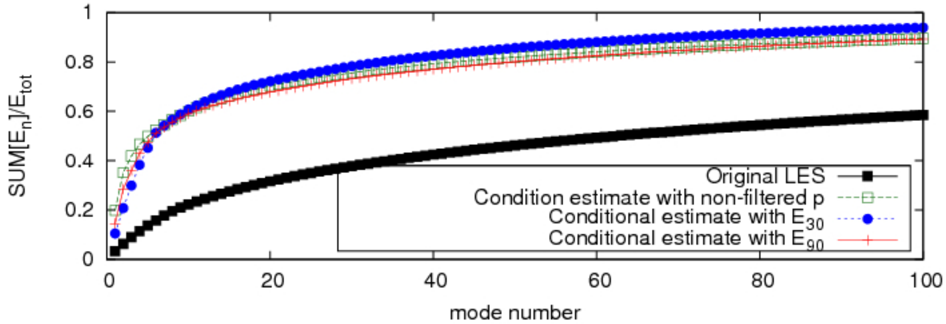

Figure 6. POD eigenspectrum for full and conditional velocity fields

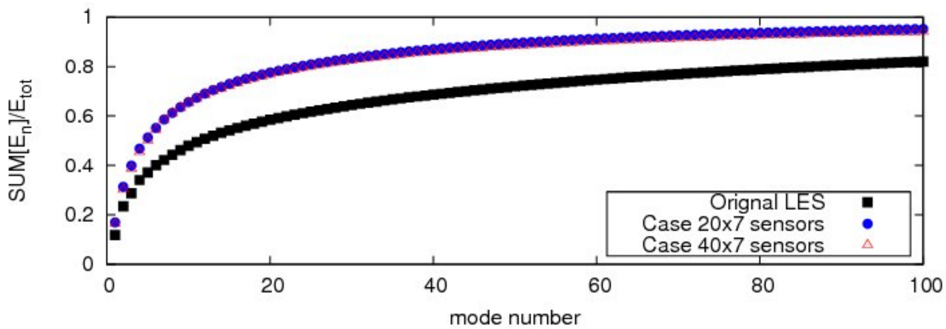

Figure 7. POD eigenspectra for the full and conditional pressure fields (in zones B and C) using different grid densities in zone A.

of which this is the signature has already been discussed: we saw in figure 5(d) how propagative disturbances released in the sideline direction are characterised by a extensive axial coherence, and this can be understood in terms of the formation of a 'bridge' between pockets of high and low pressure, carried, respectively, by saddles points and regions of coherent vortical motion. Again it is important not to loose sight of the fact that the data we analyse is issued from a Large Eddy Simulation; nevertheless, the computation provides us with a jet flow, this is dominated by large turbulence scales, and these radiate in the sideline directions. This suggests that coherent structures (often modelled as wavepackets) can produce this higher frequency sideline sound emission. Future analysis on more realistic flow data, obtained both experimental and numerically (from simulations with higher resolution and more representative upstream boundary conditions), will allow us to establish if similar radiation mechanisms exist in flows of industrial interest.

C. Source mechanism analysis

In this section we present an analysis of some short-time histories of the conditional fields, during periods when high-amplitude sound radiation is observed, in order to support the comments made earlier concerning the wavepacket type sound production which appears to underpin both downstream and sideline emissions. For the E_{30} conditional field we choose an example where the flow organisation evolves from a period of relative quiet into a period of large amplitude acoustic emission.

1. Downstream radiation

Figure 9 shows, from left to right and from top to bottom, the evolution of the E_{30} component of the acoustic field and the corresponding conditional near pressure and velocity fields. The Γ vortex identification function of Graftieaux et al[17] is used to visualise the conditional velocity field. These functions identify the location of the centre and boundary of the vortex, taking account of the local convection velocity. The algorithm used can be written, in discrete form, as

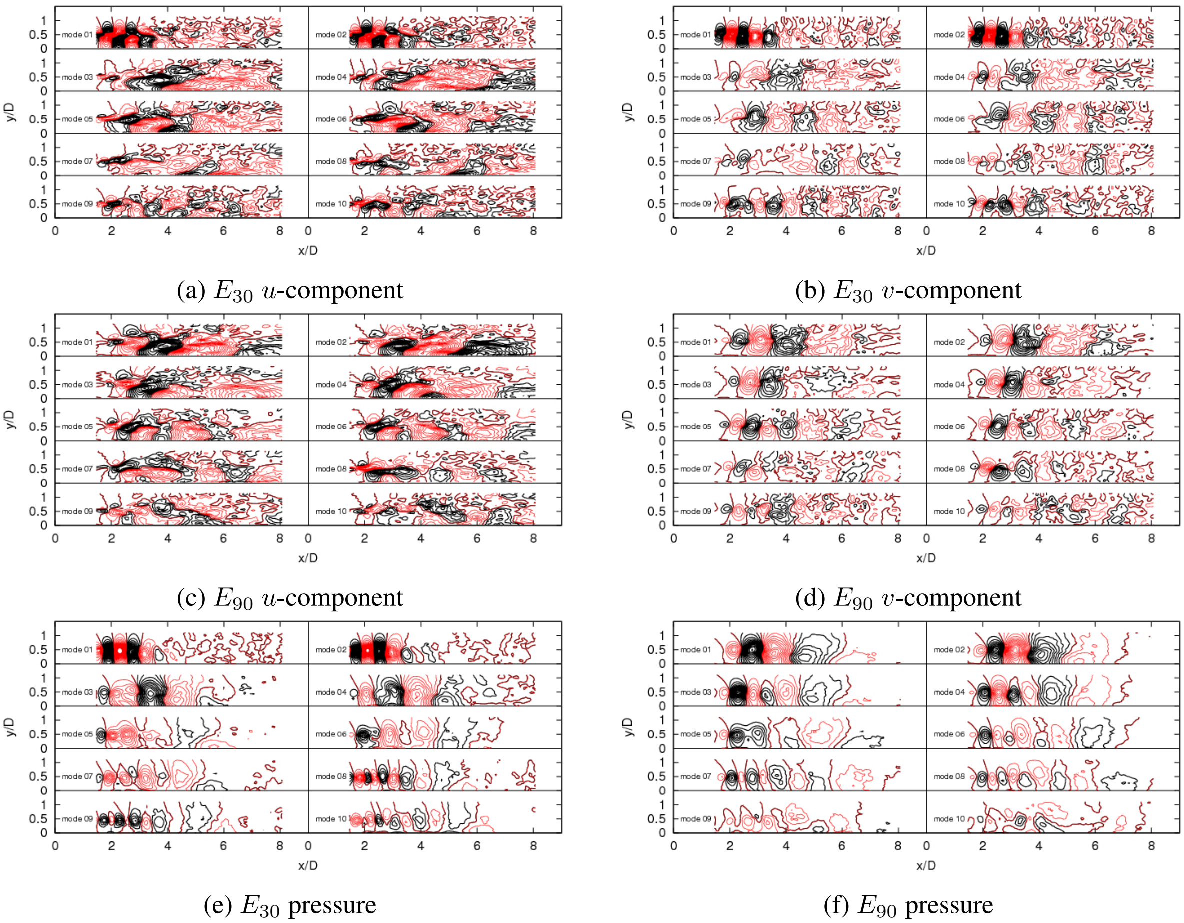

(a) E_{30} u-component

(b) E_{30} v-component

(c) E_{90} u-component

(d) E_{90} v-component

(e) E_{30} pressure

(f) E_{90} pressure

Figure 8. First ten POD eigenfunctions for E_{30} and E_{90} conditional velocity and pressure fields.

follows:

$$\Gamma(\mathrm{P}) = \frac{1}{N}\sum_{S} \frac{\left[\overrightarrow{\mathrm{PM}} \wedge (\overrightarrow{U_M} - \overrightarrow{U_p})\right] \cdot \overrightarrow{z}}{||\overrightarrow{\mathrm{PM}}|| \cdot ||(\overrightarrow{U_M} - \overrightarrow{U_p})||}, \tag{9}$$

where P denotes the point where the function is evaluated, M lies in region S centred on P–generally chosen as a rectangular area, $\vec{z}$ is the unit vector normal to the measurement plane, $\overrightarrow{U_M}$ and $\overrightarrow{U_P}$ are the velocity vectors at points M and P, respectively, and N is the number of points in S.

The conditional pressure field is shown in region B by means of a colour scale ranging from blue (negative) to red (positive) and a red iso-contour shows lines of zero pressure. This isocontour is extended into region C in order to show the conditional pressure field within the rotational region of the flow. The two events which we will illustrate are responsible for the signatures in the black time-trace which are identified by the green and red circles in figure 9(a). The green circle shows a period of relative quiet, and this is followed by a higher amplitude emission, which is identified by the red circle.

In figure 9(a) we see three coherent vortical structures, located at $x/D = 1.7, 2.5$ & 3.5. It can be seen how both the nearfield and in-flow conditional pressure fields are consistent with these three structures: low pressures are carried by the vortical cores, high pressures by the saddle points. Furthermore, the three structures are lined up on the 'lip-line' of the flow, i.e. at $y/D = 0.5$. The nearfield signature is clearly that of a wavepacket, such as have been observed experimentally by Tinney & Jordan[12] and Suzuki & Colonius[13] using nearfield microphones arrays, and which have been modelled, by means of PSE for example, by Gudmundsson & Colonius.[14] Such wavepackets can become efficient in the radiation of sound on account of spatiotemporal inhomogeneities: a localised change in space-scale, time-scale or amplitude. The evolution of the conditional flow field from figure 9(a) to (d) is predominantly convective, i.e. there is relatively little deformation of the train of coherent structures; the nearfield wavepacket signature convects accordingly, and releases only low amplitude propagative disturbances: the emission during these four time steps corresponds to the acoustic signature identified in figure 9(a) by the green circle. The evolution from sub-figure (d) to sub-figure (e) comprises an acceleration of the most downstream structure: it moves from $x/D = 4$ to $x/D = 4.4$ while the structure just upstream moves from $x/D = 2.9$ to $x/D = 3.1$. This acceleration causes the high-pressure saddle-point between the two structures to increase in axial extent, and it can be seen, in sub-figure (e), how this leads to a 'bridging' between the high-pressure of this saddle point and that of the preceding one. This kind of 'bridging' is typical of what is observed in wavepacket radiation when inhomogeneities occur, and it corresponds to a reduction in the effectiveness of the destructive interference which causes homogeneous wavepackets to be such inefficient radiators of sound; the scenario is that described by retarded-potential type descriptions of sound generation. The high-pressure 'bridge' begins to propagate (sub-figure (f)), and, immediately upstream, the low pressure zones carried by the preceding two structures form a low-pressure 'bridge' (sub-figure (g)). It is also noteworthy that the alignment of the structures on the lip-line is no longer so marked; this aspect of the breakdown in organisation of the flow structure can be expected to further degenerate the degree of destructive interference between coherent pockets of high and low pressures which would otherwise keep the flow relatively silent. As the two structures at $x/D = 2.8$ and $x/D = 3.9$ evolve from to (i) to (l) they move closer together, opening up another axially extended high pressure zone behind them, which, on account again of being imbalanced upstream and downstream, forms a bridge (constructive interference). This sequence of events leads to the higher amplitude signature, identified in sub-figure (a) by the red circle, which is released from the flow.

2. *Sideline radiation*

Figure 10 shows a short time evolution where we observe an emission, in the sideline direction, of a propagative disturbance comprising low and high pressure pulses. In sub-figure (a) blobs of vorticity can be seen at $x/D = 2.1$ and $x/D = 2.9$. The evolution from (a) to (c) comprises a growth in the spatial extent of the downstream concentration (in (c) the Γ criterion shows this as comprising two 'structures') and its associated pressure signature. The latter again 'bridges' with the pressure signature of the upstream structure to produce a radially propagating depression. While it is difficult to ascertain precisely what kind of interference mechanism is instrumental in allowing this disturbance to become propagative (in order to see this we need to examine a larger transverse extent of the flow, incorporating the opposite side of the jet; this analysis is underway), it is clear that this wave is associated with an axially extended coherent flow scale (in fact the axial extent of the wave in itself, observed in zone A, attests already to this). A positive pressure is 'squeezed' out of the saddle point which separates these structures and bridges with a large downstream high pressure. The large axial space scale manifest in the POD eigenfunctions can be associated with the foregoing scenario. We recall again that the above description must be accompanied by the caveat that this is a Large Eddy Simulation; it would be inappropriate to generalise these observations to a real high Reynolds number flow. Future work will address this point.

VI. Conclusion

We have presented an analysis methodology aimed at providing a clarification of the flow kinematics associated with downstream and sideline radiation in turbulent jets. The methodology, which has been developed and here tested using Large Eddy Simulation data, shows, for the model flow studied, how downstream radiation can be understood in terms of a wavepacket mechanism: space-time inhomogeneities, which disrupt otherwise efficient destructive interference patterns, being responsible for the production of propagative pressure disturbances.

While a similar mechanistic interpretation of the sideline radiation is not so clear, the analysis shows that the spatial flow scales associated with this component of the radiation are, for this flow, *larger* than those responsible for downstream radiation. Future application of this methodology to more realistic flow data will help establish if similar conclusions are appropriate in industrially relevant flows.

Acknowledgements

This work was partially supported by the Agence Nationale de la Recherche (ANR-05-BLAN-0208-02) through the program BruitAero. The authors would also like to acknowledge Professors B.R. Noack and T. Colonius for many helpful discussions.

References

[1] Adrian, R. J., "On the role of conditional averages in turbulent theory," *Patteson, G., Zakin, J. (Eds.), Turbulence in Liquids: Proceedings of the fourth Biennial Symposium on Turbulence in Liquids, Science Press, Princeton*, 1977, pp. 322–332.

[2] Adrian, R. J., "Conditional eddies in isotropic turbulence," *Physics of Fluids*, Vol. 22, 1979, pp. 2065–2070.

[3] Adrian, R. J., "Stochastic estimation of conditional structure: a review," *Physics of Fluids A*, Vol. 1, 1994, pp. 992–998.

[4] Bonnet, J. P., Cole, D. R., Delville, J., and Glauser, M. N., "Stochastic estimation and proper orthogonal decomposition: Complementary techniques for identifying structure," *Exp. In Fluids*, Vol. 17(5), 1994.

[5] Jordan, P., Schlegel, M., Stalnov, O., Noack, B. R., and Tinney, C., "Identifying noisy and quiet modes in jet," *13th AIAA/CEAS Aeroacoustics Conference*, Vol. Paper 2007-3602, 2007.

[6] Bogey, C. and Bailly, C., "Computation of a high Reynolds number jet and its radiated noise using large eddy simulation based on explicit filtering," *Computer and Fluids*, Vol. 35(10), 2006, pp. 1344–1358.

[7] Bogey, C., Bailly, C., and Juvé, D., "Noise investigation of a high subsonic moderate Reynolds number jet using a compressible LES," *Theor. Comput. Fluid Dyn.*, Vol. 16(4), 2003, pp. 273–297.

[8] Bogey, C. and Bailly, C., "Effects of inflow conditions and forcing on subsonic jet flows and noise," *AIAA Journal*, Vol. 43(5), 2005, pp. 1000–1007.

[9] Tam, C. K. W., Viswanathan, K., Ahuja, K. K., and Panda, J., "The sources of jet noise: experimental evidence," *J. Fluid Mech.*, Vol. 615, 2008, pp. 253–292.

[10] Jordan, P. and Gervais, Y., "Subsonic jet aeroacoustics: associating experiment, modelling and simulation," *Exp. in Fluids*, Vol. 44(1), 2008, pp. 1–21.

[11] Bogey, C. and Bailly, C., "An analysis of the correlations between the turbulent flow and the sound pressure fields of subsonic jets," *J Fluid Mech*, Vol. 583, 2007, pp. 71–97.

[12] Tinney, C. E. and Jordan, P., "The near-field pressure surrounding co-axial subsonic jets," *J. Fluid Mech.*, Vol. 611, 2008, pp. 175–204.

[13] Suzuki, T. and Colonius, T. J., "Instability waves in a subsonic jet detected using a near-field phased microphone array," *J. Fluid Mech.*, Vol. 565, 2006, pp. 197–226.

[14] Gudmundsson, K. and Colonius, T., "Parabolized stability equation models for turbulent jets and their radiated sound," *15th AIAA/CEAS Aeroacoustics Conference*, Vol. AIAA Paper 2009-3380, 2009.

[15] Sandham, N. D. and Salgado, A. M., "Nonlinear interaction model of subsonic jet noise," *Phil. Trans. Royal So. A: Math. Phys. Eng. Sci.*, Vol. 366(1876), 2008, pp. 2745–2760.

[16] Picard, C. and Delville, J., "Pressure velocity coupling in a subsonic round jet," *Heat and Fluid Flow*, Vol. 21, 2000, pp. 359–364.

[17] Graftieaux, L., Michard, M., and Grosjean, N., "Combining PIV, POD and vortex identification algorithms for the sudy of unsteady turbulent swirling flows," *Meas. Sci. Technol.*, Vol. 12, 2001, pp. 1422–1429.

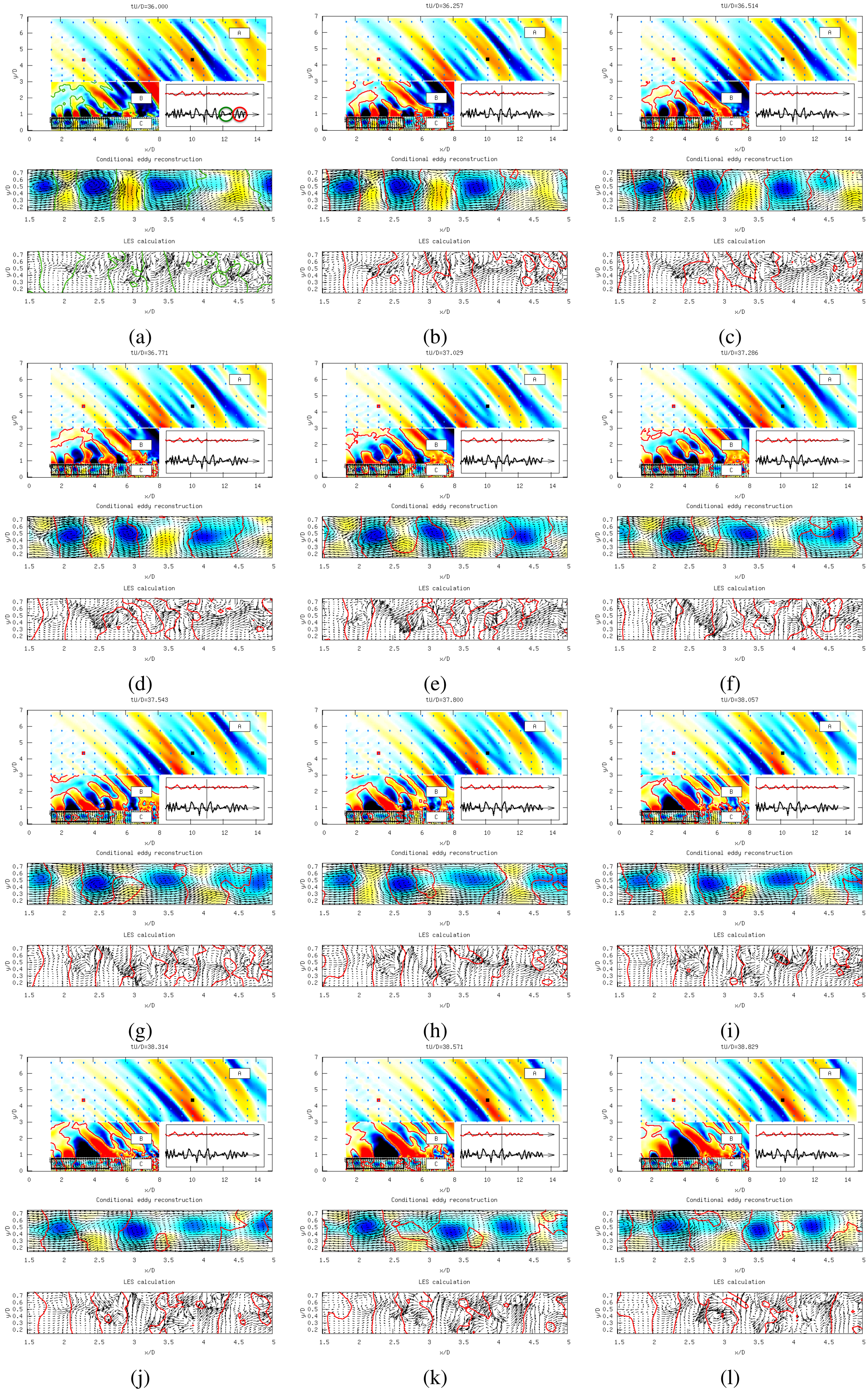

Figure 9. Short-time evolution of E_{30} acoustic field and the corresponding conditional near pressure and velocity fields. Time evolves from left to right and from top to bottom.

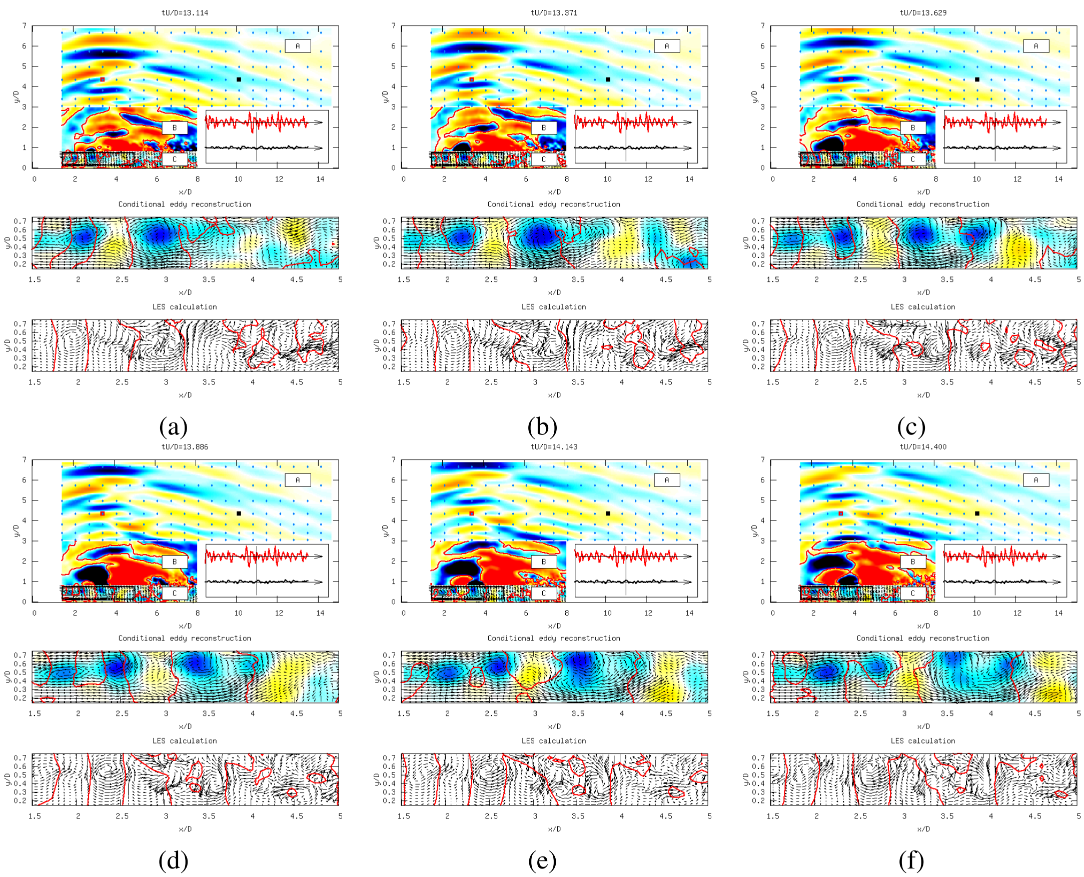

Figure 10. Short-time evolution of E_{90} acoustic field and the corresponding conditional near pressure and velocity fields. Time evolves from left to right and from top to bottom.